energies

MDPI

Article

Design and Analysis of Tubular Transverse Flux Permanent Magnet Linear Motor

Guopeng Sun [1], Mei Zhao [1,*], Jianjun Li [2,*], Tong Yao [1] and Huaqiang Zhang [1]

[1] School of Electrical Engineering and Automation, Harbin Institute of Technology, Harbin 150001, China; 23s130517@stu.hit.edu.cn (G.S.); yaotong@hit.edu.cn (T.Y.); zhq@hit.edu.cn (H.Z.)
[2] Suzhou Wise Drive Technology Co., Ltd., Suzhou 215000, China
* Correspondence: zhaomei@hit.edu.cn (M.Z.); johnson.lee@wise-drive.cn (J.L.); Tel.: +86-186-6003-8046 (M.Z.); +86-186-6256-5186 (J.L.)

Abstract: The electrical load and the magnetic load of the transverse flux permanent magnet linear motor (TFPMLM) are decoupled from each other, which makes it easy to achieve modularization, and it has broad application prospects in the field of low speed and high thrust. Firstly, the topology structure of a cylindrical TFPMLM is proposed, and its working principle is introduced. Secondly, the basic electromagnetic performance of the motor is studied. Thirdly, the influence of the structural parameters on the flux linkage, back-EFM, and cogging force has been analyzed by the 3D finite element method (FEM). Then, the kriging agent model is constructed through the DOE experiment, and a set of size parameters with better performance are found by using a multi-objective genetic algorithm. Finally, the prototype and experimental setup have been developed. The calculated results and the measured results are in good agreement.

Keywords: transverse flux permanent magnet linear motor; multi-objective optimization; electromagnetic characteristics; finite element

check for updates

Citation: Sun, G.; Zhao, M.; Li, J.; Yao, T.; Zhang, H. Design and Analysis of Tubular Transverse Flux Permanent Magnet Linear Motor. *Energies* **2024**, *17*, 6180. https://doi.org/10.3390/en17236180

Academic Editor: Lorand Szabo

Received: 6 October 2024
Revised: 16 November 2024
Accepted: 4 December 2024
Published: 7 December 2024

Copyright: © 2024 by the authors. Licensee MDPI, Basel, Switzerland. This article is an open access article distributed under the terms and conditions of the Creative Commons Attribution (CC BY) license (https://creativecommons.org/licenses/by/4.0/).

1. Introduction

The transverse flux permanent magnet linear motor (TFPMLM) is a special motor with high thrust density [1–5]. The armature winding and the stator slot are perpendicular to each other in space due to their transverse flux structure, which can realize the respective design of magnetic and electric loads to improve the performance of the motor. The decoupling of each phase is also convenient for independent control. In addition, the TFPMLM also makes it easy to realize the modularity. Hence, the TFPMLM has broad prospects in applications as varied as robotics [6,7], electrical power generation [8,9], electromagnetic launcher [10–12], and transportation [13]. Basic structure of TFPMLM is shown in Figure 1.

In recent years, plenty of topology structures have emerged. The flux-switching TFPMLM is put forward in reference [14]. The windings and PMs are installed in the same part of the machine. This motor type synthesizes the characteristics of a flux-switching permanent magnet linear motor, and it has the advantages of high efficiency, high thrust density, and bipolar flux linkage [15]. A transverse flux cylindrical linear synchronous motor using generic armature cores for rotary machinery is proposed to address the problem of complex structures in the conventional TFPMLM [16–18]. However, the thrust density of this motor still needs to improve. The authors in [10] proposed a cylindrical TFPMLM structure. This kind of motor has large thrust force, a simple structure, and high mechanical strength, but the problems of large magnetic leakage and low power factor still exist. A cylindrical staggered tooth structure TFPMLM which has achieved a low force ripple of 2.78% and high force density is proposed in [19,20]. This kind of motor has solved the problem of large magnetic leakage between motor poles. Ref. [21] proposed a TFPMLM that has low armature magnetic leakage and a high power factor and thrust

density due to its special magnetic circuit structure and PM design. However, irreversible demagnetization occurred during the installation process due to the complex structure of PM, and the performance of the final prototype was significantly different from the theoretical value.

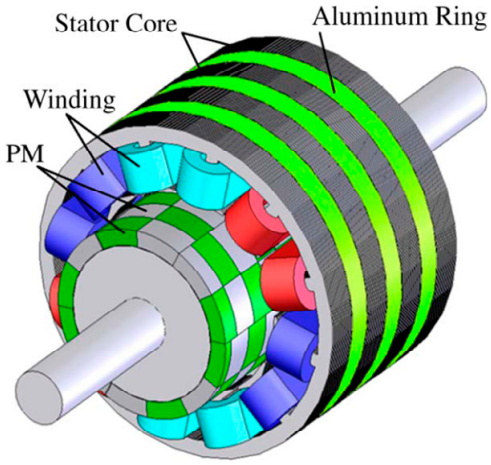


Figure 1. Basic structure of TFPMLM. Reproduced with permission of [10], copyright of ©2011 IEEE.

Current research on the TFPMLM mainly focuses on innovation of the motor topology and improvement in the EM performance, while research on the multi-objective optimization of the motor's complex 3D structure and its application in oil field exploitation is very limited. In this paper, the EM performance and multi-objective optimization design of the TFPMLM will be carried out according to the design requirements of the submersible linear motor.

This paper is organized as follows: the construction and work principle of a novel TFPMLM are introduced in Section 2. The 3D finite element model is established, and the EM characteristics of the motor are studied in Section 3. Section 4 discusses the influence of the key size parameters of the motor on the thrust, cogging force, and back-EMF. The kriging agent model is constructed through the DOE experiment in Section 5, and a set of size parameters with better performance are found by using the multi-objective genetic algorithm. The prototype and back-EMF measurements are presented in Section 6. The conclusions are summarized in Section 7.

2. The Construction and Principle of TFPMLM

2.1. Structure of TFPMLM

The 3D model of the TFPMLM studied in this paper is shown in Figure 2. The TFPMLM adopts a 12-slot circular three-phase structure. The secondary design is shown in Figure 3. The number of salient pole teeth in the circumferential direction of the secondary is consistent with the primary, and both the windings and the secondary magnetic conductive teeth need to be staggered by one-third of the pole pitch. The PMs with a dual alternating pole structure are distributed on both sides of the primary and secondary, and the permanent magnet is radially magnetized. More details are given in [22]. This article focuses on the field of submersible oil, considering the impact of harsh underground environments on motor structures; the initial values of the main parameters and parameter marks of the TFPMLM are shown in Table 1 and Figure 4, respectively.

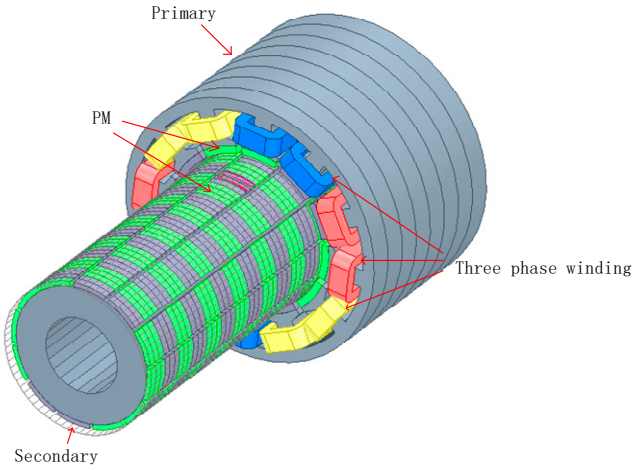


Figure 2. Three-dimensional finite element model of TFPMLM.

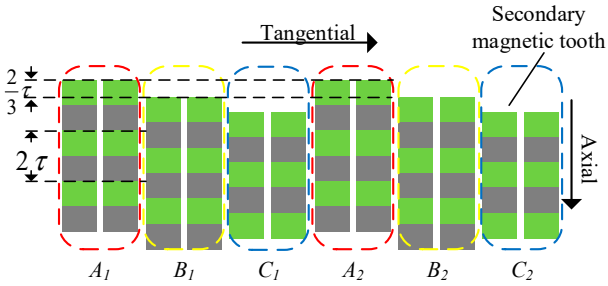


Figure 3. The arrangement of the secondary magnetic conductive teeth.

Table 1. Initial value of TFPMLM parameters.

Parameter	Symbol	Value
Outer radius of primary iron core	R_{po}	52 mm
Primary slot height	h_{pt}	10.8 mm
Axial length of primary PM	l_{pm}	8 mm
Primary yoke height	h_{py}	5 mm
Primary tooth width	w_{pt}	7 mm
Air gap	g	1 mm
Radius of secondary cylinder	R_{so}	27.4 mm
Axial length of secondary PM (pole distance)	τ	9 mm
Inner radius of secondary iron core	R_{si}	15 mm
Primary PM height	h_{PM}	3 mm
Secondary PM height	h_{st}	3 mm
Secondary pole arc coefficient	α_{st}	0.8
Primary slot width	w_{po}	3.5 mm

2.2. Working Principle of Generator

In essence, the TFPMLSM is a kind of variable-reluctance motor that relies on the modulation of the primary permanent magnet excitation source and the secondary poles to alternately change the flux linkage in the armature windings, thus generating an inductive potential and electromagnetic force. Based on the principle of magnetic field modulation, the magnetic field analysis is carried out below [22]. And the back electromotive force and electromagnetic thrust are derived.

To simplify the derivation process, the following assumptions need to be made:

(1) The impact of iron core saturation is ignored;
(2) The eddy current losses and hysteresis losses are excluded;
(3) The magnetic field only changes in the radial direction.

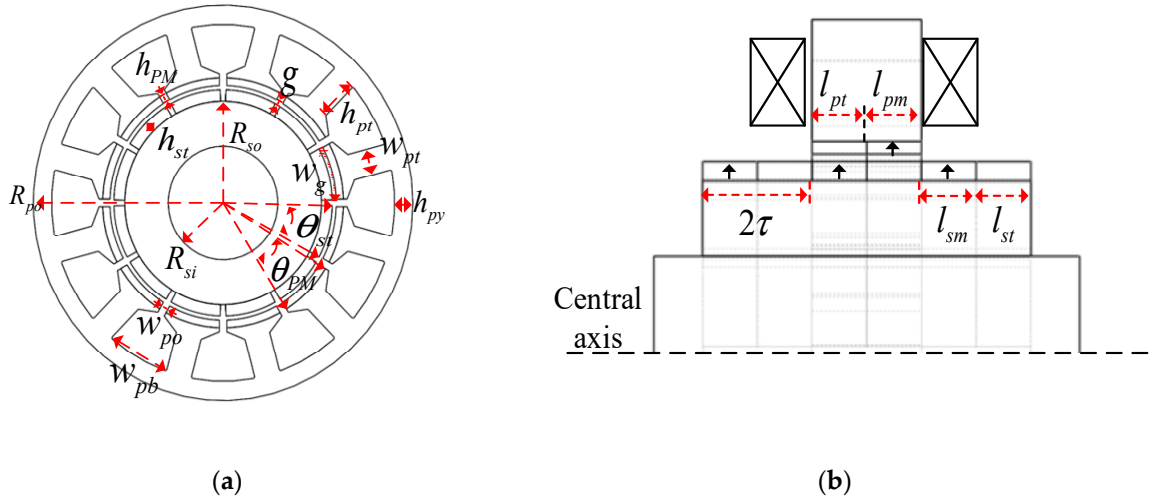


Figure 4. Size parameters of motor. (**a**) Front of motor; (**b**) side of motor.

Due to the presence of permanent magnets on both sides of the primary and secondary sides of the transverse flux submersible permanent magnet linear motor, and the alternating arrangement of permanent magnets and guide magnet teeth, when analyzing the air gap magnetic density, it can be decomposed into two sets of magnetic flux models: primary permanent magnet and secondary iron core, and secondary permanent magnet and primary iron core. As shown in Figure 5, (c) and (e) correspond to the secondary magnetic flux teeth and primary permanent magnet in (a), and (d) and (f) correspond to the primary magnetic flux teeth and secondary permanent magnet in (b), respectively. By calculating the air gap flux density separately for two sets of magnetomotive force permeability models, the overall air gap flux density expression is obtained by superimposing them.

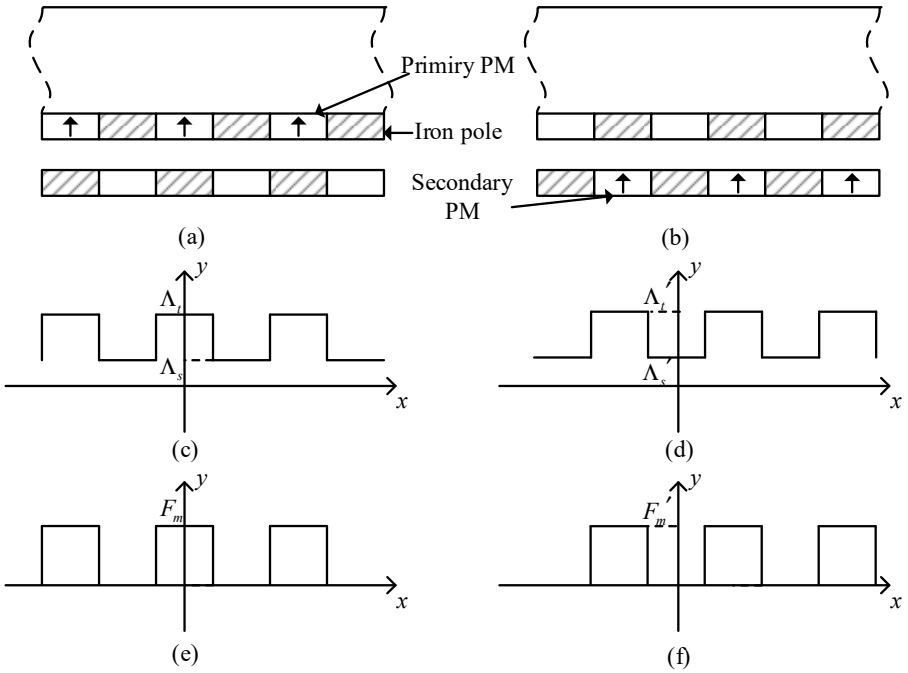


Figure 5. MMF distribution of PMs and permeance distribution of iron poles. (**a**) Modal of primary PMs and secondary iron poles; (**b**) modal of secondary PMs and primary iron poles; (**c**) permeance of secondary iron poles; (**d**) permeance of primary iron poles; (**e**) MMF of primary PMs; (**f**) MMF of secondary PMs.

In Figure 5, Λ_t represents the permeance per unit area of the secondary iron pole:

$$\Lambda_t = \frac{1}{h_{pm} + g} \tag{1}$$

The permeance per unit area between the iron poles can be expressed as follows:

$$\Lambda_s = \frac{1}{h_{pm} + g + h_{st}} \tag{2}$$

The Fourier series form of the permeance waveform shown in Figure 5c is as follows:

$$\begin{aligned} &\Lambda(x,t) = \Lambda_0 + \sum_{i=1}^{\infty} \Lambda_i \cos[\frac{\pi i}{\tau}(x - vt)] \\ &\Lambda_0 = \frac{\mu_0}{\tau}(\Lambda_t l_{st} + \Lambda_s l_{sp}) = \mu_0(\frac{1}{h_{pm} + g} + \frac{1}{h_{pm} + g + h_{st}}) \\ &\Lambda_i = \frac{2\mu_0}{i\pi}(\Lambda_t - \Lambda_s)\sin(\frac{i\pi l_{st}}{2\tau}) = \frac{2\mu_0}{i\pi}(\frac{1}{h_{pm} + g} - \frac{1}{h_{pm} + \delta + h_{st}})\sin(\frac{i\pi}{2}) \end{aligned} \tag{3}$$

where Λ_0 is the DC component in the secondary permeance, Λ_i is the harmonic coefficient of each order of secondary permeance, and v is the moving speed of the secondary.

Similarly, the Fourier series form of the MMF of primary PMs shown in Figure 5e is as follows:

$$\begin{aligned} &F_{pm}(x) = F_0 + \sum_{i=1}^{\infty} F_i \cos(\frac{\pi i}{\tau}x) \\ &F_0 = \frac{F_m l_{pm}}{T} = \frac{B_r h_{pm}}{2\mu_0} \\ &F_i = \frac{2}{T}\int_0^T f(x)\cos(\frac{2\pi i x}{T})dx = \frac{B_r h_{pm}}{i\pi\mu_0}\sin(\frac{i\pi}{2}) \end{aligned} \tag{4}$$

where F_0 is the DC component in the MMF of primary PMs. F_i is the harmonic coefficient MMF of primary PMs.

The MMF waveform of secondary PMs and the permeance waveform of primary iron poles are exactly 180° different from the MMF of primary PMs and the permeance of secondary iron poles. Therefore, the MMF of secondary PMs can be expressed as follows:

$$\begin{aligned} &F_{sm}(x,t) = F_0' + \sum_{i=1}^{\infty} F_i' \cos[\frac{\pi}{\tau}(x - vt)] \\ &F_0' = \frac{F_m' l_{sm}}{T} = \frac{B_r h_{st}}{2\mu_0} \\ &F_i' = \frac{2}{T}\int_0^T f(x)\cos(\frac{2\pi i x}{T})dx = \frac{B_r h_{st}}{i\pi\mu_0}\sin(\frac{i\pi}{2}) \end{aligned} \tag{5}$$

where F_0' is the DC component in the MMF of secondary PMs. F_i' is the harmonic coefficient of the MMF of the secondary PMs.

Similarly, the primary permeance can be expressed as follows:

$$\begin{aligned} &\Lambda(x)' = \Lambda_0' - \sum_{i=1}^{\infty} \Lambda_i' \cos(\frac{\pi i}{\tau}x) \\ &\Lambda_0' = \mu_0(\frac{1}{h_{st} + g} + \frac{1}{h_{pm} + g + h_{st}}) \\ &\Lambda_i' = \frac{2\mu_0}{i\pi}(\Lambda_t' - \Lambda_s')\sin(\frac{i\pi l_{pt}}{2\tau}) = \frac{2\mu_0}{i\pi}(\frac{1}{h_{st} + g} - \frac{1}{h_{pm} + g + h_{st}})\sin(\frac{i\pi}{2}) \end{aligned} \tag{6}$$

where Λ_0' is the DC component in the primary permeance. Λ_i' is the harmonic coefficient of each order of primary permeance.

The expression of the air gap flux density at no-load by ignoring the influence of higher-order harmonics can be obtained as follows [22]:

$$\begin{aligned} B_g(x,t) &= F_{pm}(x)\Lambda(x,t) + F_{sm}(x,t)\Lambda'(x) \\ &= F_0\Lambda_0 + F_0{}'\Lambda_0{}' + (F_1\Lambda_0 - F_0{}'\Lambda_1{}')\cos\tfrac{\pi x}{\tau} \\ &+ (F_0\Lambda_1 - F_1{}'\Lambda_0{}')\cos\tfrac{\pi}{\tau}(x - vt) + (F_1\Lambda_1 + F_1{}'\Lambda_1{}')\cos\tfrac{\pi x}{\tau}\cos\tfrac{\pi}{\tau}(x - vt) \end{aligned} \tag{7}$$

From Equation (7), it can be seen that the first and second terms are the DC components generated by the primary and secondary permanent magnets, respectively. These components do not change with time or the motion of the secondary, and their magnitude is only related to the permanent magnet and its magnetic permeability. The third component is directly generated by the interaction between the permanent magnets attached to the primary and secondary stages and therefore does not change with the movement of the motor secondary. Therefore, it cannot generate induced electromotive force in the armature winding. Due to the modulation effect of the primary and secondary convex pole iron core teeth on the magnetic field of the permanent magnet, the fourth and fifth harmonic magnetic field components in the equation are generated, which are related to time and the relative motion between the primary pole.

According to the law of electromagnetic induction, only magnetic flux that is interlocked with the winding and alternates with time will generate induced potential. The TFPMSLM circular three-phase structure has four sets of coils connected in series for each phase, thus obtaining a single-phase winding magnetic flux:

$$\phi_{ph} = 4p\int_{-\tau}^{\tau} B_g(x,t)w_g dx = 4pw_g\tau(F_1\Lambda_1 + F_1{}'\Lambda_1{}')\cos\frac{\pi vt}{\tau} \tag{8}$$

where p is the polar logarithm.

By taking the derivative of the total magnetic flux, the expression for the no-load back electromotive force of the motor can be obtained:

$$e = \frac{d\psi}{dt} = \frac{dN\phi_{ph}}{dt} = \frac{4pNw_gB_rv}{\pi}\left(\frac{h_{pm}}{h_{pm}+g} + \frac{h_{st}}{h_{st}+g} - \frac{h_{pm}+h_{st}}{h_{pm}+h_{st}+g}\right)\sin\frac{\pi vt}{\tau} \tag{9}$$

where N is the number of turns in the winding.

If the interaction coefficient between the primary permanent magnet and the secondary permanent magnet is k_{ps}, then

$$k_{ps} = \frac{h_{pm}}{h_{pm}+g} + \frac{h_{st}}{h_{st}+g} - \frac{h_{pm}+h_{st}}{h_{pm}+h_{st}+g} \tag{10}$$

If the effective value of the fundamental wave of the back electromotive force is e_0, then

$$e_0 = \frac{2\sqrt{2}pN\omega_gB_rvk_{ps}}{\pi} \tag{11}$$

The three-phase windings of the TFPMSLM are staggered by 120 electrical angles in the circumferential direction, so the three-phase back electromotive force can be expressed as follows:

$$\begin{aligned} e_a &= \sqrt{2}e_0\sin\tfrac{\pi}{\tau}vt \\ e_b &= \sqrt{2}e_0\sin(\tfrac{\pi}{\tau}vt - \tfrac{2\pi}{3}) \\ e_c &= \sqrt{2}e_0\sin(\tfrac{\pi}{\tau}vt + \tfrac{2\pi}{3}) \end{aligned} \tag{12}$$

The TFPMSLM circumferential three-phase is independent of each other. In order to reduce the influence of the direct axis armature reaction on the demagnetization effect of the permanent magnet, improve the current control efficiency, and obtain the maximum electromagnetic thrust, a control strategy of $i_d = 0$ is adopted. A current in the same phase

as the opposite potential is applied to each phase winding, that is, the power factor cosφ = 1. At this time, the output power equation of the motor is

$$P_o = \frac{m}{T}\int_0^{2T} e(t)i(t)dt = me_0 i_0 \tag{13}$$

where m is the number of phases in the motor. T is the electric cycle. i_0 is the effective value of the single-phase winding current.

Under the condition of ignoring high-order harmonics and only considering the fundamental wave, the output electromagnetic force of the motor can be expressed as follows:

$$F_{em} = \frac{P_0}{v} = \frac{me_0 i_0}{v} \tag{14}$$

Substituting Equation (11) into Equation (14) yields the following:

$$F_{em} = \frac{P_0}{v} = \frac{2\sqrt{2}mpN\omega_g B_r i_0 k_{ps}}{\pi} \tag{15}$$

3. Electromagnetic Characteristics of TFPMLM

The magnetic coupling between the three phases is negligible due to the independent magnetic circuit structure of the TFPMLM, so that the single-phase model can be used for the finite element calculation. The one-sixth unit motor model is used to increase the computation speed, as shown in Figure 6.

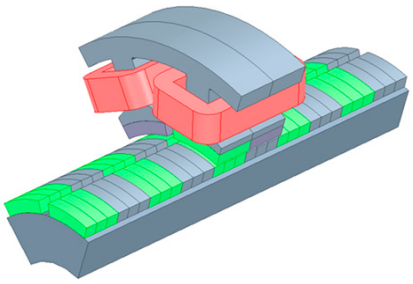
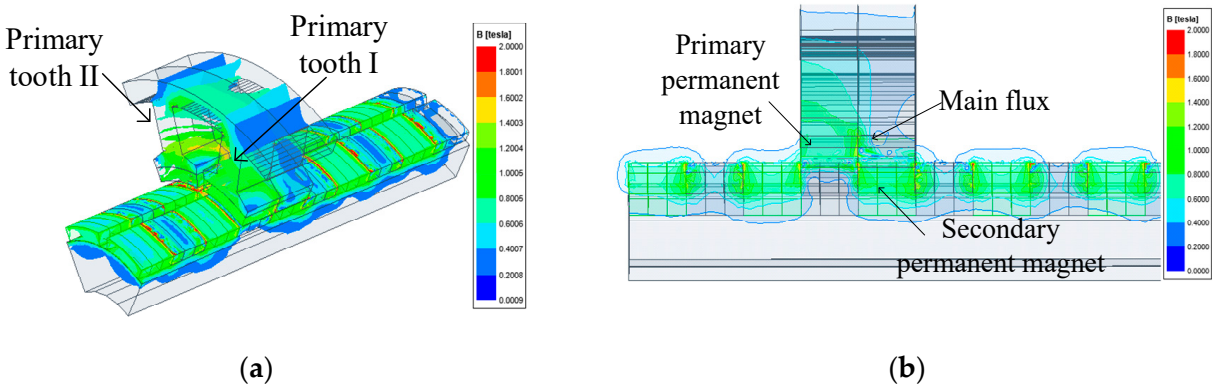


Figure 6. Three-dimensional finite element model of TFPMLM.

3.1. No-Load Magnetic Field

Figures 7 and 8 show the flux distribution of the motor at no load. The magnetic fields at the primary teeth I and II are complementary and symmetrical because the motor model is symmetrical, and the PM and the magnetic conductive teeth are alternately arranged. Only the magnetic field at the primary tooth I needs to be analyzed.



(**a**) (**b**)

Figure 7. Flux distribution at no load. (**a**) Amplitude of flux linkage is maximum; (**b**) x = 0.

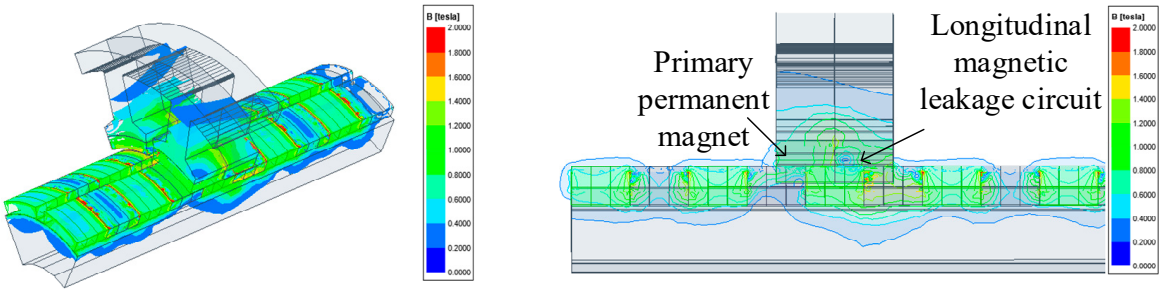


Figure 8. Flux distribution at no load. (**a**) Amplitude of flux linkage is 0; (**b**) x = τ/2.

Figure 7a shows the flux distribution of the secondary at the initial position. At the moment of x = 0, the magnetic flux under the primary tooth I goes to the primary tooth II circumferentially along the yoke and reaches the maximum value. When the secondary moves a distance of τ/2, the alignment of the primary and secondary PMs under tooth II is the same as that of tooth I; thus, the two magnetic fluxes cancel each other. As shown in Figure 8a, the net magnetic flux interlinked with the windings is zero at this time. Figures 7a and 8a present that the main magnetic flux of the stator mainly flows between the two teeth and does not intersect with other phases, which verifies the decoupling between the three phases.

Figures 7b and 8b show the flux distribution on the side of the TFPMLM. At x = 0, the primary permanent magnet and the secondary permanent magnet are offset by a pole distance in the direction of motion. At this time, the magnetic flux generated by the secondary permanent magnet does not directly pass through the air gap vertically upward to reach the primary iron core teeth but most of the magnetic flux first reaches the S pole of the primary permanent magnet along the axial air gap. This is because the magnetization direction of the primary and secondary permanent magnets is the same, and there is an attractive force between them. Therefore, some of the magnetic flux generated by the secondary permanent magnet will be attracted by the primary permanent magnet, first reaching the primary permanent magnet, then passing through the primary iron core teeth to reach the other side of the primary iron core teeth in the circumferential direction, and then returning to the secondary iron core through the air gap to form the main magnetic flux circuit.

3.2. No-Load Flux Linkage and Back-EMF

The no-load flux linkage in an electrical period is shown in Figure 9. It can be seen that the waveform of the flux linkage has a good sinusoid. Figure 9b presents the harmonic distribution of the A-phase flux linkage. It can be seen that the harmonics are dominated by the third harmonic, whose amplitude is 0.35 mWb, accounting for 4% of the fundamental wave.

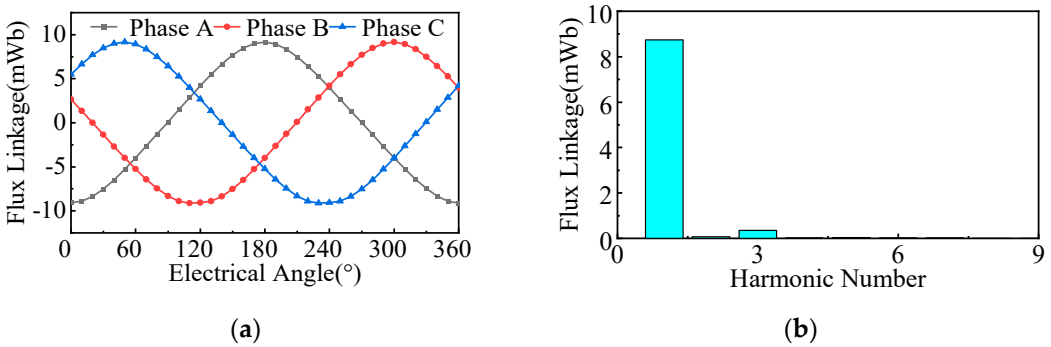


Figure 9. Winding flux linkage and harmonics. (**a**) Waveforms; (**b**) harmonic components.

The back-EMF waveform of the motor in an electrical period is shown in Figure 10a. It can be seen that the winding back-EMF waveform is a flat top wave. Figure 10b presents the harmonic components of the back-EMF.

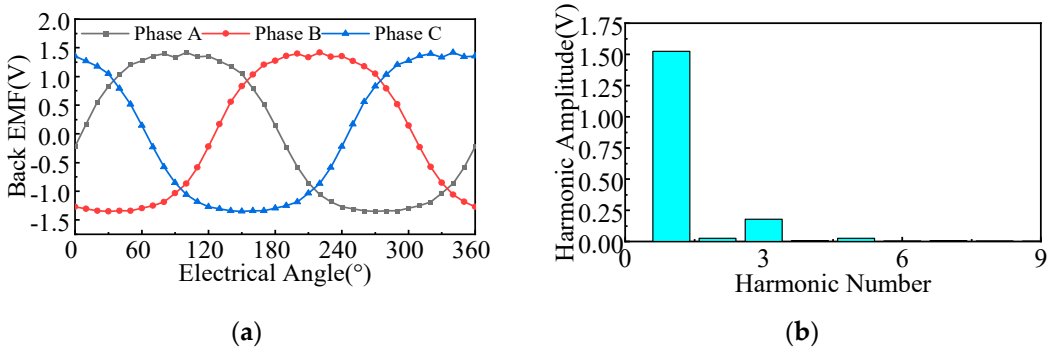


Figure 10. Back-EMF and harmonics. (**a**) Waveforms; (**b**) harmonic components.

3.3. Cogging Force and Electromagnetic Thrust

The normal components of the cogging force can cancel each other due to the cylindrical structure of the TFPMLM and the symmetrical distribution of three-phase windings; thus, only the cogging force along the direction of motion needs to be considered. The cogging force waveform of the TFPMLM is shown in Figure 11. It can be seen that the single-phase cogging force pulsates once in a slot range, and the peak-to-peak value is 9.25 N. The synthesized three-phase cogging force is shown in Figure 11a, and Figure 11b presents the harmonic components of the single-phase cogging force. It can be seen that the three-phase cogging force fluctuates three times in an electrical period. Furthermore, the total cogging force is greatly suppressed, and its peak-to-peak value is 5.5 N.

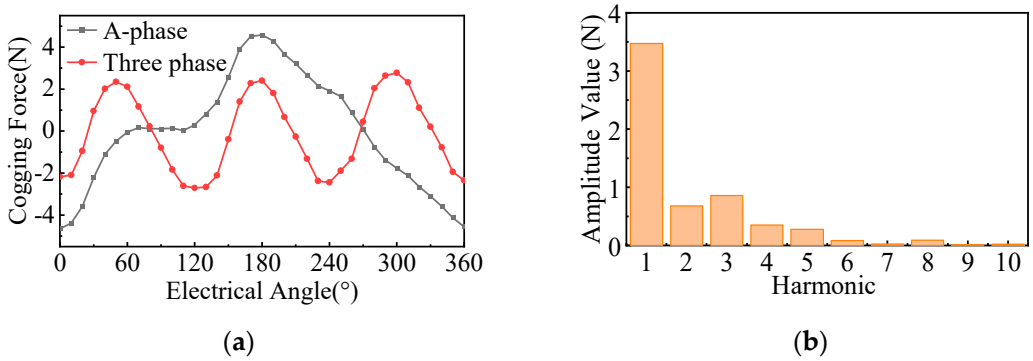


Figure 11. Cogging force and harmonics. (**a**) Waveforms; (**b**) harmonic components.

With a three-phase alternating current through the windings, the thrust density distribution under different armature magnetomotive forces (MMFs) is obtained, as shown in Figure 12a. It can be found that with the increase in the armature MMF, the thrust density of the motor gradually increases. The thrust density tends to be saturated when the armature MMF is about 750 A.

Figure 12b presents the waveform thrust density of the unit motor versus the armature MMF. It can be found that the fluctuation frequency of the single-phase thrust is the same as that of the input current. By adopting the circular three-phase structure, the amplitude of the three-phase thrust is larger, and the fluctuation is smaller than the single-phase.

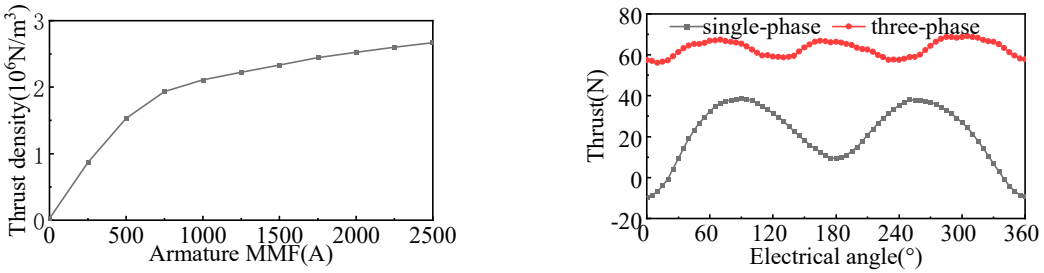


Figure 12. EM thrust. (**a**) Thrust density versus armature MMF; (**b**) single-phase and three-phase EM thrust.

4. Single Objective of TFPMLM

In this section, the influence of the main parameters on the flux linkage and back-EMF is analyzed, and the optimization range is determined to provide a reference for the multi-objective optimization design.

4.1. Influence of Main Structural Parameters on Flux Linkage and Back-EMF

Figures 13 and 14 show the influence of the radial length of the primary and secondary PMs (h_{PM} and h_{st}) on the flux linkage and back-EMF. It can be seen that the influence of the h_{PM} and h_{st} on the flux linkage and the back-EMF is the same. Therefore, just the h_{PM} needs to be studied.

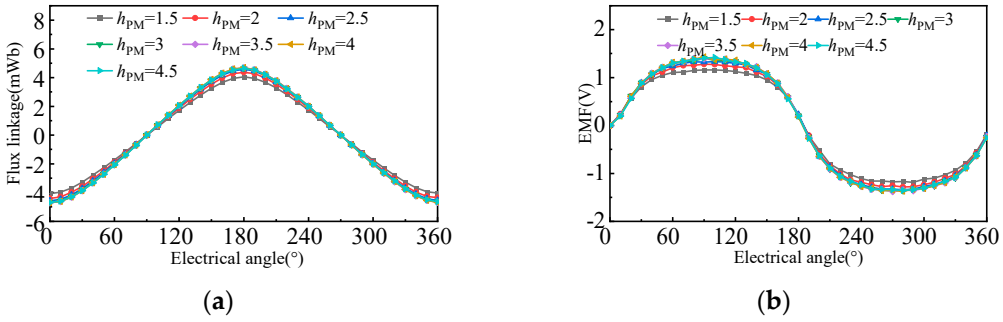


Figure 13. Flux linkage and back-EMF versus h_{PM}. (**a**) Flux linkage; (**b**) back-EMF.

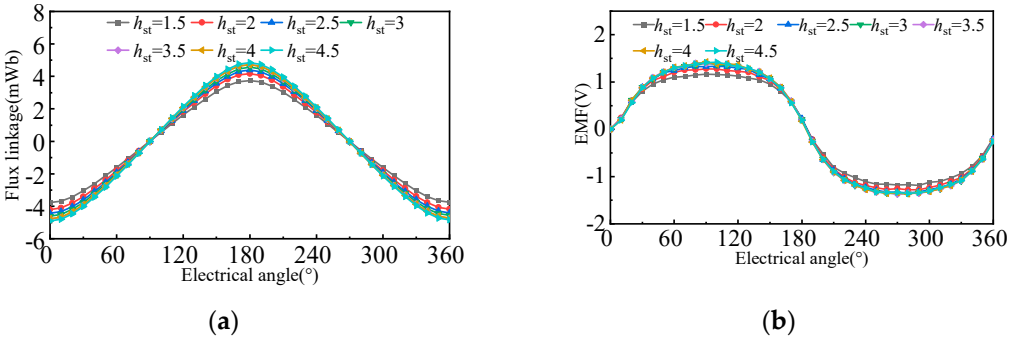
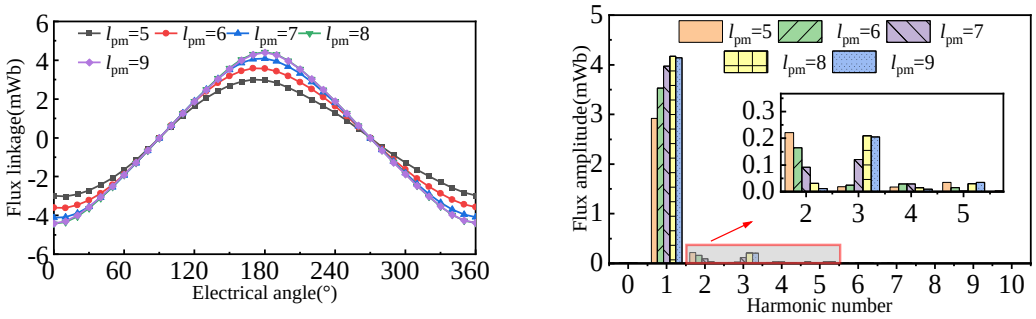


Figure 14. Flux linkage and back-EMF versus h_{st}. (**a**) Flux linkage; (**b**) back-EMF.

As shown in Figure 13a, with the increase in the radial length of the PM, the flux linkage amplitude increases and gradually tends to be saturated. Figure 13b shows the waveform of back-EMF versus h_{PM}. Compared with Figure 13a, the influence of h_{PM} on back-EMF and flux linkage is consistent. A compromised radial length of PM in the range of 1.5 mm to 4 mm is adopted considering that the length of the PM has a huge influence on the PM consumption and the manufacturing cost.

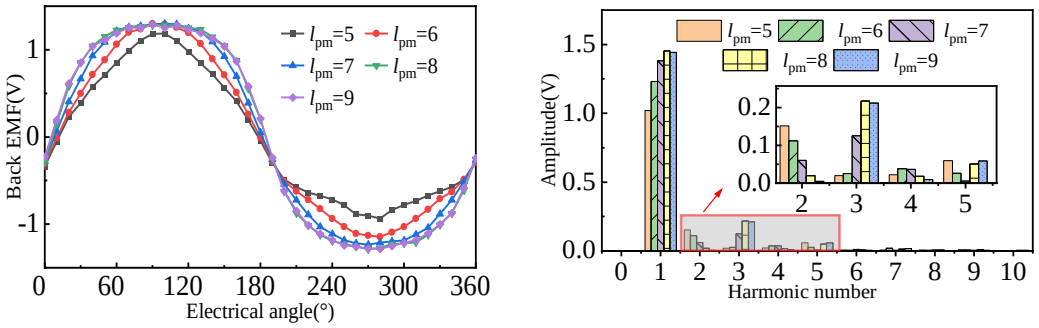
For further analysis, the influence of the axial length of primary PM (l_{pm}) on flux linkage and back-EMF is analyzed. The speed of the mover is 1 m/s. Figure 15 presents the winding flux linkage and its harmonic components versus l_{pm}. It can be found that with the increase in l_{pm}, the amplitude of the flux linkage increases and tends to be stable when l_{pm} is close to the pole distance.



(**a**) (**b**)

Figure 15. Flux linkage versus l_{pm}. (**a**) Waveforms; (**b**) harmonic components.

Figure 16 shows the waveforms of the back-EMF and its harmonic versus l_{pm}. Compared with Figure 15, it can be concluded that the influence of l_{pm} on the back-EMF is the same as that of the flux linkage. The third harmonic content increases and the back-EMF waveform gradually becomes a flat-top wave with the increase in l_{pm}.



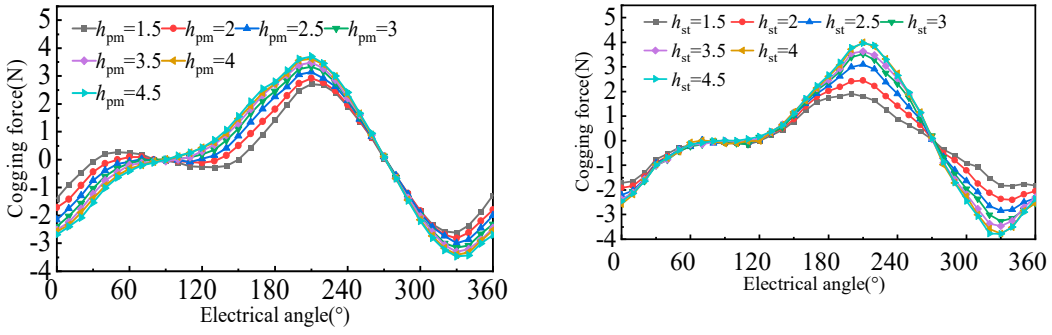
(**a**) (**b**)

Figure 16. Back-EMF versus l_{pm}. (**a**) Waveforms; (**b**) harmonic components.

4.2. Influence of Main Structural Parameters on Cogging Force

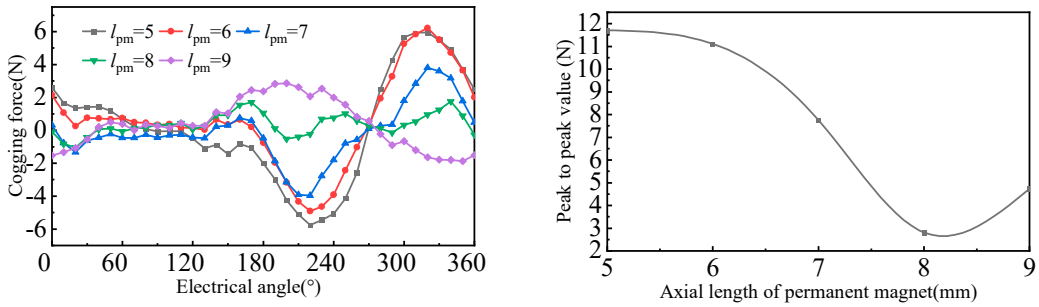
Firstly, the influence of the h_{PM} and h_{st} on the cogging force is studied, as shown in Figure 17. It can be found that the influence of h_{PM} and h_{st} on the amplitude of the cogging force is consistent. The longer the axial length of the PM, the greater the peak-to-peak value of the cogging force.

Subsequently, the influence of l_{pm} on the cogging force is studied, as shown in Figure 18. Figure 18a presents that the peak-to-peak cogging force decreases first and then increases along with the increase in l_{pm}. Figure 18b presents that the minimum value 2.8 N is obtained when l_{pm} = 8 mm. Figure 19 shows the harmonic components of cogging force and its amplitude value versus l_{pm}. It can be found that the fundamental wave and the second and third harmonic amplitudes first decrease then increase with the increase in l_{pm}. The minimum value is obtained at l_{pm} = 8 mm.



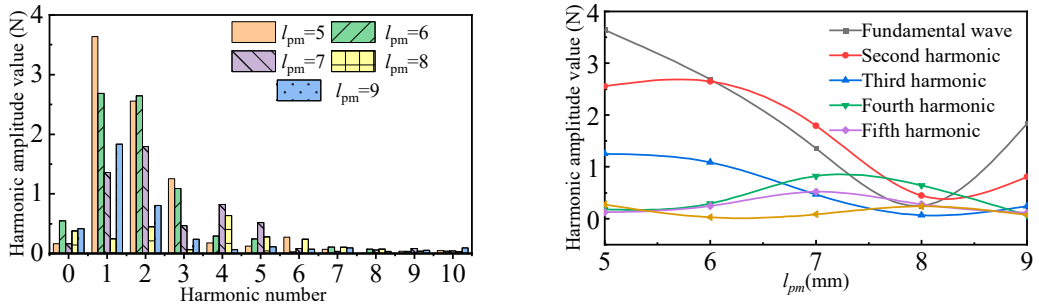
(**a**) (**b**)

Figure 17. Cogging force versus radial lengths of PMs. (**a**) Radial length of primary PM (h_{PM}); (**b**) radial length of secondary PM (h_{st}).



(**a**) (**b**)

Figure 18. Single-phase cogging force and its peak-to-peak value versus l_{pm}. (**a**) Cogging force; (**b**) peak-to-peak value.



(**a**) (**b**)

Figure 19. Harmonic components of cogging force and its amplitude value versus l_{pm}. (**a**) Harmonic components; (**b**) harmonic amplitude.

5. Multi-Objective Optimization of TFPMLM

The multi-objective optimization process is shown in Figure 20.

Firstly, the mathematical model of optimal design is established. Secondly, the DOE experiment is designed through the optimal space filling method to establish the initial sample database. Thirdly, the kriging agent model is established. Finally, the multi-objective genetic algorithm is used to iteratively optimize the kriging agent model to obtain the Pareto frontier solution.

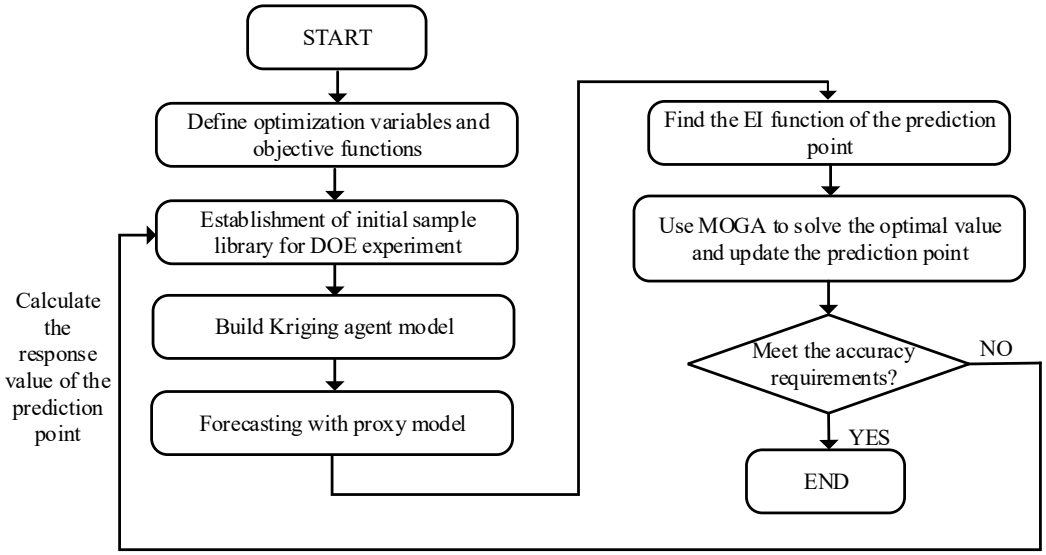


Figure 20. Multi-objective optimization design process.

5.1. Establishment of Mathematical Model

The optimized structural parameters and their variation ranges are shown in Table 2:

Table 2. Initial value and range of design variables.

Parameter	Symbol	Initial Value	Variation Range [L, U]
Primary PM height/mm	h_{PM}	3	1.5~4.5
Primary slot opening width/mm	w_{po}	2.5	2.5~5
Secondary PM height/mm	h_{st}	3	1.5~4.5
Secondary pole arc coefficient	α_{st}	0.8	0.5~0.9

The optimization objectives are as follows.

5.1.1. Thrust Density F_{pm}

The increase in thrust density is beneficial to improving the utilization rate of PMs. In this paper, thrust density is defined as the ratio of the thrust to the volume of the PM:

$$F_{\mathrm{pm}} = \frac{F}{V_{\mathrm{pm}}} \tag{16}$$

5.1.2. Back-EMF Fundamental Amplitude E_1

The increase in the back-EMF is beneficial to the improvement in the thrust force. The Fourier expression of the fundamental amplitude of back-EMF is edited in Electronics Desktop as an output variable.

5.1.3. Back-EMF Waveform Distortion Rate *THD*

The *THD* is an index to measure the sine degree of back-EMF. The smaller the *THD*, the fewer the harmonics. The mathematical expression of *THD* can be expressed as

$$THD = \frac{\sqrt{E_2E_2 + E_3E_3 + E_4E_4 + \cdots E_{\mathrm{n}}E_{\mathrm{n}}}}{E_1} \tag{17}$$

where E_{n} is the amplitude of the nth harmonic of the back-EMF.

5.1.4. Peak-to-Peak Value of Cogging Force F_{cog}

Since the cogging force has a significant impact on the motor efficiency and control effect, the F_{cog} should be minimized.

The mathematical model of the TFPMLM optimization design can be expressed as

$$\begin{cases} \text{Find } X = [h_{\text{PM}}\ w_{\text{po}}\ h_{\text{st}}\ \alpha] \\ \max F_{\text{pm}}(X) = F_{\text{m}} \\ \max E_1(X) = E_{1\text{m}} \\ \min F_{\text{cog}}(X) = F_{\text{cogn}} \\ \min THD(X) = THD_{\text{n}} \\ s.t.: \text{L} \leq X \leq \text{U} \end{cases} \tag{18}$$

where X is the value space of the design variables, and L and U are the upper and lower limits of the value space. F_{m} and $E_{1\text{m}}$ are the maximum values of thrust density and fundamental wave amplitude of back-EMF, respectively. F_{cogn} and THD_{n} are, respectively, the peak-to-peak value of the cogging force and the minimum back-EMF distortion rate.

5.2. DOE Experiment Design

The Optimal Space-Filling Design (OSF) method was used to establish 25 sampling points for the four optimization variables in the DOE experiment, and the response of the sampling points was computed by 3D FEM. The experimental arrangement and its optimized target response values are shown in Table 3:

Table 3. Experimental arrangement and single-phase unit generator response value of OSF method.

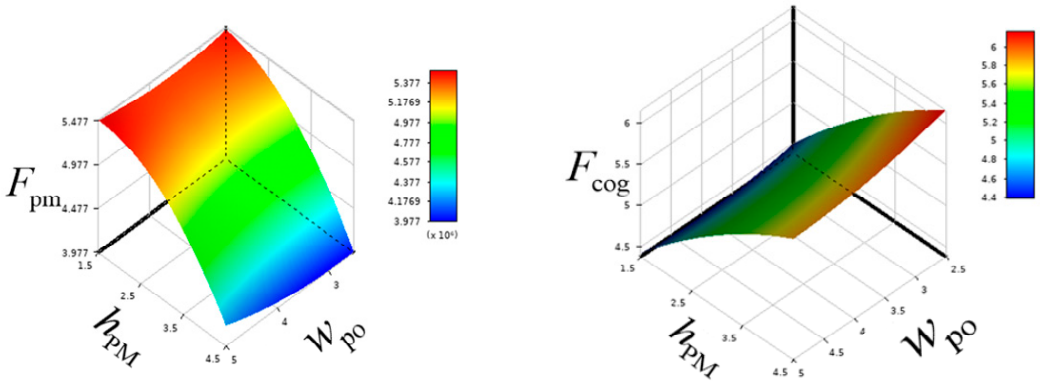
	Design Variable				**Optimization Objectives**			
	h_{PM} **(mm)**	h_{st} **(mm)**	α_{st}	w_{po} **(mm)**	F_{cog} **(N)**	E_1 **(V)**	THD	F_{pm} **(10^6N/m^3)**
1	3.24	2.76	0.51	3.75	3.73	0.97	0.13	3.90
2	3.60	3.36	0.67	3.30	5.70	1.32	0.13	4.36
3	1.68	3.00	0.84	3.10	5.64	1.40	0.15	5.04
4	3.00	3.60	0.90	3.60	7.54	1.63	0.13	4.57
5	1.56	4.08	0.68	4.00	5.05	1.18	0.15	4.73
6	3.96	2.16	0.54	4.60	3.63	0.95	0.13	3.89
7	2.64	3.96	0.76	2.50	6.59	1.51	0.13	5.06
8	4.44	2.52	0.65	3.45	5.08	1.20	0.13	4.06
9	4.20	3.84	0.64	4.30	5.86	1.25	0.13	3.88
10	1.92	3.24	0.86	4.70	5.99	1.36	0.15	5.21
11	3.84	3.72	0.52	2.60	4.84	1.08	0.13	3.47
12	2.40	2.64	0.70	3.80	4.51	1.25	0.14	5.59
13	2.80	4.50	0.60	3.50	5.37	1.22	0.13	4.29
14	3.72	2.40	0.83	2.80	5.90	1.49	0.14	4.74
15	3.12	4.32	0.78	4.50	6.90	1.47	0.13	4.76
16	4.32	4.20	0.80	3.20	7.83	1.56	0.12	4.08
17	4.08	2.88	0.81	4.40	6.48	1.43	0.13	4.51
18	3.48	2.04	0.62	2.70	3.98	1.10	0.14	4.26
19	2.16	1.68	0.72	2.95	3.18	1.11	0.15	5.88
20	1.80	3.12	0.59	3.00	3.90	1.06	0.14	5.10
21	2.88	2.28	0.75	4.90	4.73	1.24	0.14	5.10
22	2.52	3.48	0.56	4.86	4.34	1.06	0.13	4.86
23	2.30	1.90	0.88	4.00	4.29	1.31	0.15	4.84
24	2.04	1.80	0.57	4.20	2.64	0.89	0.15	5.31
25	3.36	1.56	0.73	3.90	3.70	1.13	0.15	5.45

5.3. Kriging Agent Model

The kriging agent model of the TFPMLM about the optimization objective is constructed, and the kriging response surface is obtained.

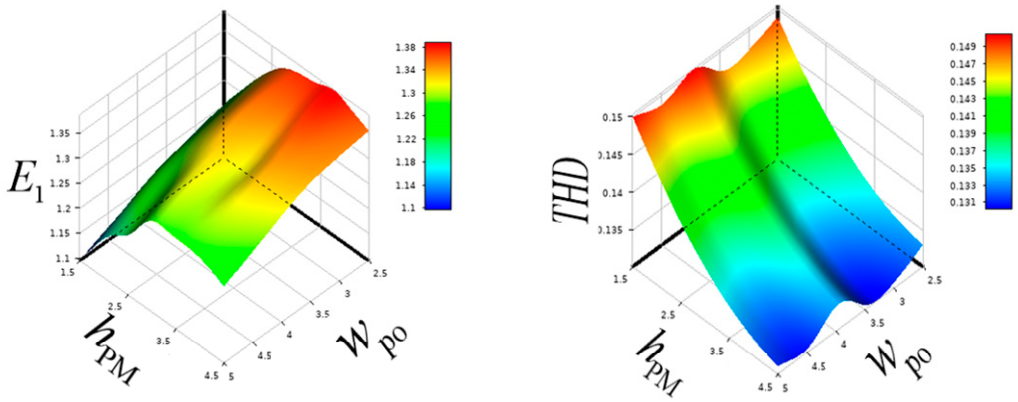
Figures 21 and 22 present the response of different optimization objectives versus the h_{PM} and w_{po}. It can be seen that the F_{pm}, F_{cog}, and THD vary monotonously with the increase in h_{PM}. It is worth noting that there is an optimal h_{PM} that yields the maximum

E_1. The F_{pm} and F_{cog} decrease with the increase in w_{po}, and the E_1 and *THD* are not monotonously changing. Therefore, the benefit of optimal w_{po} selection has to consider these optimization objectives comprehensively.



(**a**) (**b**)

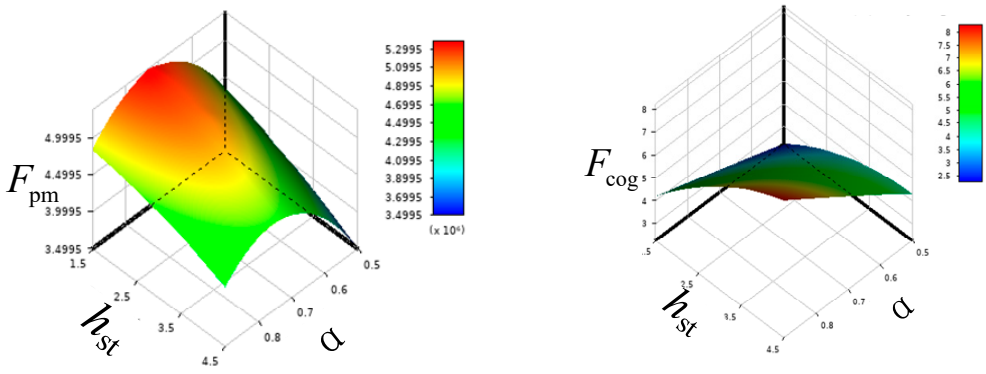
Figure 21. Response of optimization target versus h_{PM} and w_{po}. (**a**) F_{pm}; (**b**) F_{cog}.



(**a**) (**b**)

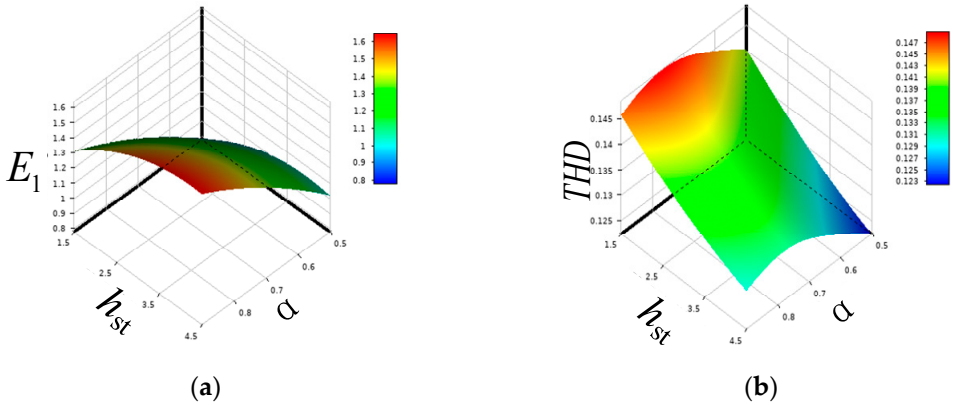
Figure 22. Response of optimization target versus h_{PM} and w_{po}: (**a**) E_1; (**b**) *THD*.

Figures 23 and 24 show the responses of different optimization objectives under h_{st} and α_{st}. It can be found that with the increase in the h_{st}, F_{cog} and E_1 increase monotonically, and the F_{pm} and THD decrease monotonically. With the increase in α_{st}, the F_{cog} and E_1 gradually increased, while the F_{pm} and *THD* first increased and then decreased.



(**a**) (**b**)

Figure 23. Response of optimization target versus h_{st} and α. (**a**) F_{pm}; (**b**) F_{cog}.

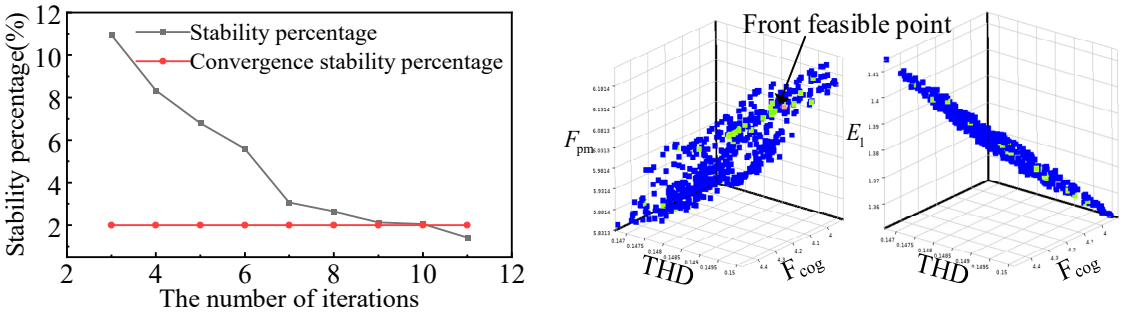


(**a**) (**b**)

Figure 24. Response of optimization target versus h_{st} and α. (**a**) E_1; (**b**) *THD*.

5.4. Multi-Objective Genetic Algorithm Optimization

The multi-objective genetic algorithm (MOGA) used in this paper is based on the non-dominated sorting genetic algorithm II (NSGA-II). The number of samples per iteration and the iteration convergence stability are set to 800 and 2%, respectively. The algorithm iteration trend and Pareto front are obtained through the MOGA, as shown in Figure 25. It can be seen from Figure 25a that the stability percentage of the optimization algorithm reaches the convergence value after 11 iterations. Figure 25b shows the Pareto frontier of the population after optimization.



(**a**) (**b**)

Figure 25. Iterative convergence trend of MOGA and Pareto frontier. (**a**) MOGA iteration convergence; (**b**) Pareto frontier.

5.5. Optimization Results

Table 4 shows the comparison of the structural design.

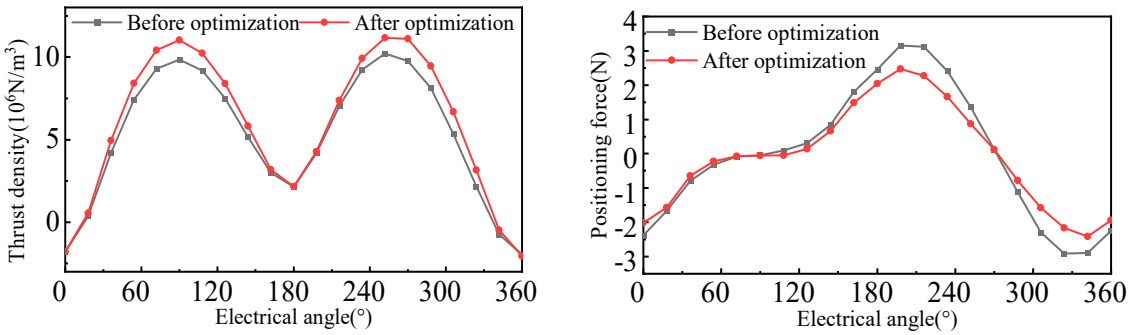
Table 4. Comparison of structural design.

	h_{PM} (mm)	h_{st} (mm)	α_{st} (mm)	w_{po} (mm)
Before optimization	3	3	0.8	3.5
After optimization	2.8	1.8	0.9	2.6
Difference	−0.2	−1.2	0.1	−0.9

The waveforms of each optimization target before and after optimization are shown in Figure 26, and the numerical indicators of each optimization objective are shown in Table 5.

It can be seen from Table 5 that the thrust density of the TFPMLM is increased by 13.1% after optimization, while the peak-to-peak value of the cogging force is reduced by 19.34%. On the other hand, the amplitude of back-EMF is slightly reduced, and the *THD* is slightly increased. This is due to the reduction in the h_{PM} and h_{st} results in the reduction in

PM usage. However, the relative difference is within the expected tolerance range, which can meet the design requirements.



(**a**) (**b**)

Figure 26. Comparison of optimization target waveforms. (**a**) Single-phase thrust density; (**b**) single-phase cogging force.

Table 5. Comparison of performance data.

Optimization Objectives	Before Optimization	After Optimization	Difference	Relative Variation/%
$F_{pm}(10^6\mathrm{N/m^3})$	5.21	5.90	0.798	13.1
F_{cog} (N)	6.0475	4.878	−1.1695	−19.34
E_1 (V)	1.4756	1.4375	−0.0381	−2.58
THD (%)	13.72	14.68	0.96	7.00

6. Experiment and Analysis Results

6.1. Experiment Platform

The simulation optimizations mentioned above pertain to the one-sixth unit model, as depicted in Figure 6. The three-phase, four-unit TFPMLM and the experimental platform are illustrated in Figure 27.

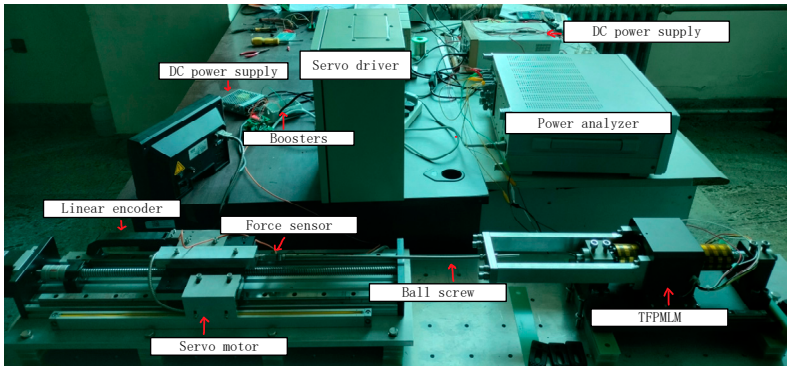


Figure 27. Prototype experiment platform.

6.2. Back-EMF Measurement

Figure 28 shows a snapshot of the back-EMF measurement for the three-phase, four-unit TFPMLM, and the full-model back-EMF diagram of the motor by FEM is given in Figure 29. In this experiment, the armature winding of the TFPMLM is connected to a power analyzer, and the servo driver is programmed to control the servo motor to drive the primary of the TFPMLM to move at a constant speed of 0.486 m/s. The back electromotive force data are obtained through the power analyzer. It should be noted that the experimental motor speed is 0.486 m/s while the simulation motor speed is 0.072 m/s. The result is thus converted to a unit speed of 1 m/s. A comparison of the waveforms of

the simulation and the experiment is given in Figure 30. The maximum error between the simulation and experiment is less than 10%, as Figure 30 illustrates. It can be found that the experiment result is in accordance with the FEM.

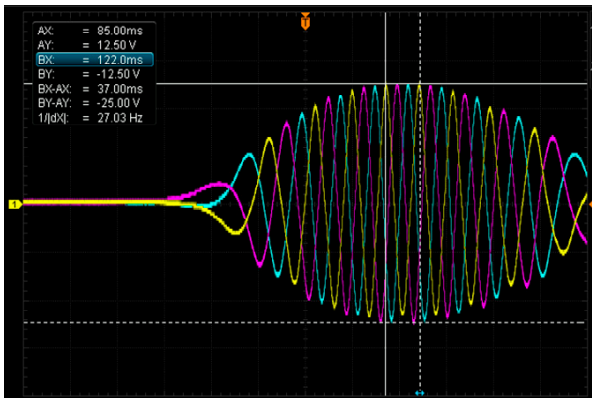


Figure 28. No-load back-EMF by experiment.

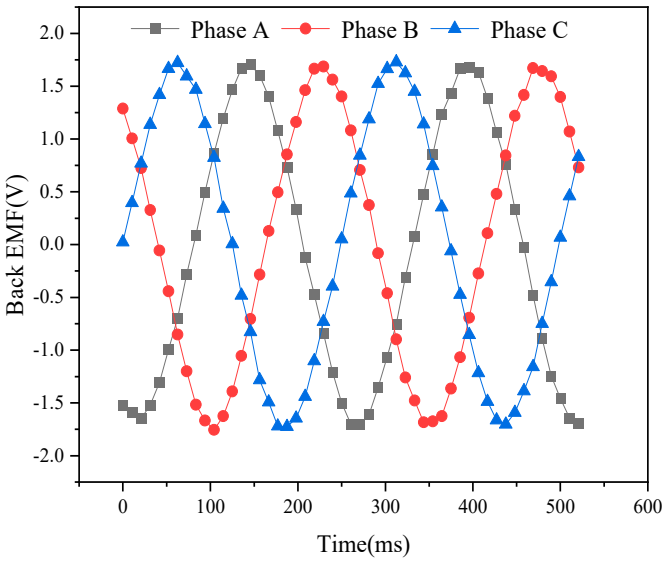


Figure 29. No-load back-EMF by FEM.

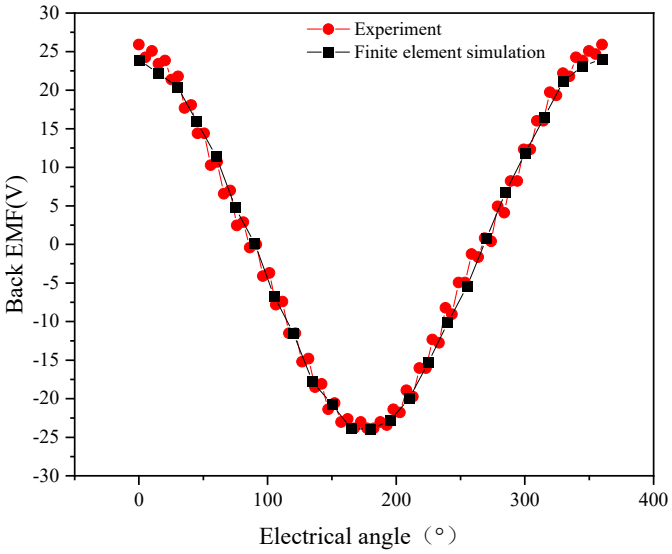


Figure 30. Comparison of no-load back-EMF by experiment and FEM.

7. Conclusions

The novel double alternating pole TFPMLM was proposed in this paper.

(1) The basic structure and working principle of the TFPMLM are described. The electromagnetic characteristics of flux linkage, back-EMF, cogging force, and thrust of the motor under constant velocity motion are analyzed.
(2) The 3D model of the motor is established, and the magnetic field distribution characteristics of the motor are explained. The electromagnetic characteristics of flux linkage, back-EMF, cogging force, and thrust of the motor are analyzed. After that, the influence of key size parameters on the electromagnetic characteristics of the TFPMLM is revealed. The results present that the optimal height range of primary and secondary PMs is 1.5–4 mm, the leakage coefficient shows an obvious inflection point at a pole distance of 9 mm, and the minimum of the peak-to-peak cogging force that appears in the axial length of primary PMs ranges from 8 mm to 9 mm.
(3) This experiment is arranged by the OSF method, and the motor kriging agent model is constructed, and a set of parameters with excellent performance are obtained by iterating the agent model by MOGA. The results show that the motor thrust density is improved by 13.1% and the cogging force is reduced by 19.34% after optimization.
(4) The prototype of the TFPMLM has been built, and the experiment results show that the experiment result is in accordance with the finite element method.

Author Contributions: Conceptualization, M.Z.; methodology, M.Z.; software, G.S. and J.L.; validation, J.L.; formal analysis, G.S., M.Z. and J.L.; investigation, H.Z.; data curation, J.L., T.Y. and G.S.; writing—original draft, G.S. writing—review and editing, T.Y.; visualization, H.Z.; supervision, J.L.; project administration, H.Z. and J.L. All authors have read and agreed to the published version of the manuscript.

Funding: This work was supported in part by the National Natural Science Foundation of China under Project 52177032 and the Aviation Science Foundation (ASFC-20230007077004).

Data Availability Statement: The original contributions presented in the study are included in the article, further inquiries can be directed to the corresponding authors.

Conflicts of Interest: The authors declare no conflicts of interest. The funders had no role in the design of the study; in the collection, analyses, or interpretation of the data; in the writing of the manuscript; or in the decision to publish the results.

References

1. Luo, J.; Kou, B.; Yang, X.; Zhang, H.; Zhang, L. Development, Design, and Analysis of a Dual-Consequent-Pole Transverse Flux Linear Machine for Direct-Drive Applications. *IEEE Trans. Ind. Electron.* **2021**, *68*, 6097–6108. [CrossRef]
2. Zhao, M.; Wei, Y.; Yang, H.; Xu, M.; Han, F.; Deng, G.; Hou, D.; Zhang, P. Development and Analysis of Novel Flux-Switching Transverse-Flux Permanent Magnet Linear Machine. *IEEE Trans. Ind. Electron.* **2019**, *66*, 4923–4933. [CrossRef]
3. Kou, B.; Luo, J.; Yang, X.; Zhang, L. Modeling and Analysis of a Novel Transverse-Flux Flux-Reversal Linear Motor for Long-Stroke Application. *IEEE Trans. Ind. Electron.* **2016**, *63*, 6238–6248. [CrossRef]
4. Wang, Q.; Zhao, B.; Zhao, H.; Li, Y.; Zou, J. Optimal Design of Tubular Transverse Flux Motors With Low Cogging Forces for Direct Drive Applications. *IEEE Trans. Appl. Supercond.* **2016**, *26*, 0609005. [CrossRef]
5. Jia, Z.; Chen, W.; Yu, L.; Cai, J.; Jia, H. A Novel Transverse-Flux PM Linear Machine With Double Ω-Hoop Stator. *IEEE Trans. Appl. Supercond.* **2016**, *26*, 0612404. [CrossRef]
6. Smadi, I.A.; Omori, H.; Fujimoto, Y. Development, Analysis, and Experimental Realization of a Direct-Drive Helical Motor. *IEEE Trans. Ind. Electron.* **2012**, *59*, 2208–2216. [CrossRef]
7. Fujimoto, Y.; Kominami, T.; Hamada, H. Development and Analysis of a High Thrust Force Direct-Drive Linear Actuator. *IEEE Trans. Ind. Electron.* **2009**, *56*, 1383–1392. [CrossRef]
8. Wang, J.; Wang, W.; Jewell, G.W.; Howe, D. A Low-Power, Linear, Permanent-Magnet Generator/Energy Storage System. *IEEE Trans. Ind. Electron.* **2002**, *49*, 640–648. [CrossRef]
9. Colli, V.D.; Cancelliere, P.; Marignetti, F.; Di Stefano, R.; Scarano, M. A Tubular-Generator Drive For Wave Energy Conversion. *IEEE Trans. Ind. Electron.* **2006**, *53*, 1152–1159. [CrossRef]
10. Zhao, M.; Zou, J.; Xu, Y.; Zou, J.; Wang, Q. The Thrust Characteristic Investigation of Transverse Flux Tubular Linear Machine for Electromagnetic Launcher. *IEEE Trans. Plasma Sci.* **2011**, *39*, 925–930. [CrossRef]

11. Zou, J.; Zhao, M.; Wang, Q.; Zou, J.; Wu, G. Development and Analysis of Tubular Transverse Flux Machine With Permanent-Magnet Excitation. *IEEE Trans. Ind. Electron.* **2012**, *59*, 2198–2207. [CrossRef]
12. Zhao, J.; Mou, Q.; Guo, K.; Liu, X.; Li, J.; Guo, Y. Reduction of the Detent Force in a Flux-Switching Permanent Magnet Linear Motor. *IEEE Trans. Energy Convers.* **2019**, *34*, 1695–1705. [CrossRef]
13. Suzuki, K.; Kim, Y.-J.; Dohmeki, H. Driving Method of Permanent-Magnet Linear Synchronous Motor With the Stationary Discontinuous Armature for Long-Distance Transportation System. *IEEE Trans. Ind. Electron.* **2012**, *59*, 2227–2235. [CrossRef]
14. Lu, Q.F.; Li, Y.X.; Huang, X.Y.; Ye, Y.Y. Analysis of Transverse-Flux Linear Switched-Flux Permanent Magnet Machine. *IEEE Trans. Magn.* **2015**, *51*, 8108804. [CrossRef]
15. Cao, R.; Cheng, M.; Zhang, B. Speed Control of Complementary and Modular Linear Flux-Switching Permanent-Magnet Motor. *IEEE Trans. Ind. Electron.* **2015**, *62*, 4056–4064. [CrossRef]
16. Shin, J.-S.; Watanabe, R.; Koseki, T.; Kim, H.-J. Practical Design Approach of a Transverse Flux Linear Synchronous Motor for Compact Size, Small Mover Weight, High Efficiency, and Low Material Cost. *IEEE Trans. Magn.* **2015**, *51*, 8200504. [CrossRef]
17. Shin, J.-S.; Watanabe, R.; Koseki, T.; Kim, H.-J. Transverse-Flux-Type Cylindrical Linear Synchronous Motor Using Generic Armature Cores for Rotary Machinery. *IEEE Trans. Ind. Electron.* **2014**, *61*, 4346–4355. [CrossRef]
18. Shin, J.-S.; Koseki, T.; Kim, H.-J. Transverse Flux Type Cylindrical Linear Synchronous Motor for Large Thrust Using Generic Armature Cores for Rotary Machinery. In Proceedings of the 2012 XXth International Conference on Electrical Machines, Marseille, France, 2–5 September 2012; IEEE: Marseille, France, 2012; pp. 795–800.
19. Zheng, P.; Zhu, S.; Yu, B.; Cheng, L.; Fan, Y. Analysis and Optimization of a Novel Tubular Staggered-Tooth Transverse-Flux PM Linear Machine. *IEEE Trans. Magn.* **2015**, *51*, 8111304. [CrossRef]
20. Sui, Y.; Yin, Z.; Wang, M.; Yu, B.; Zheng, P. A Tubular Staggered-Teeth Transverse-Flux PMLM with Circumferentially Distributed Three-Phase Windings. *IEEE Trans. Ind. Electron.* **2019**, *66*, 4837–4848. [CrossRef]
21. Arshad, W.M.; Thelin, P.; Backstrom, T.; Sadarangani, C. Use of Transverse-Flux Machines in a Free-Piston Generator. *IEEE Trans. Ind. Appl.* **2004**, *40*, 1092–1100. [CrossRef]
22. Zhao, M.; Li, Y.; Zuo, S.; Tang, P.; Yao, T.; Zhang, H.; Wu, S. Electromagnetic Vibration Analysis of Transverse Flux Permanent Magnet Linear Submersible Motor for Oil Production. *Energies* **2023**, *16*, 7911. [CrossRef]

Disclaimer/Publisher's Note: The statements, opinions and data contained in all publications are solely those of the individual author(s) and contributor(s) and not of MDPI and/or the editor(s). MDPI and/or the editor(s) disclaim responsibility for any injury to people or property resulting from any ideas, methods, instructions or products referred to in the content.